

Differential and Integral Cross Sections of the $\text{N}(^2\text{D}) + \text{H}_2 \rightarrow \text{NH} + \text{H}$ Reaction from Exact Quantum and Quasi-Classical Trajectory Calculations

Shi Ying Lin,[†] Luis Bañares,[‡] and Hua Guo^{*,†}

Department of Chemistry, University of New Mexico, Albuquerque, New Mexico 87131, and Departamento de Química Física I, Facultad de Química, Universidad Complutense, 28040 Madrid, Spain

Received: December 1, 2006; In Final Form: January 23, 2007

Exact quantum mechanical state-to-state differential and integral cross sections and their energy dependence have been calculated on an accurate NH_2 potential energy surface (PES), using a newly proposed Chebyshev wave packet method. The NH product is found to have a monotonically decaying vibrational distribution and an inverted rotational distribution. The product angular distributions peak in both forward and backward directions, but with a backward bias. This backward bias is more pronounced than that observed previously on a less accurate PES. Both the differential and integral cross sections oscillate mildly with collision energy, indicating the dominance of short-lived resonances. The quantum mechanical results are compared with those obtained from quasi-classical trajectories. The agreement is generally reasonable and the discrepancies can be attributed to the neglect of quantum effects such as tunneling. Detailed analysis of the trajectories revealed that the backward bias in the differential cross section stems overwhelmingly from the fast insertion component of the reaction, augmented with some flux from the abstraction channel, particularly at high collision energies.

I. Introduction

The $\text{N}(^2\text{D}) + \text{H}_2$ ($X\ ^1\Sigma_g^+$) \rightarrow NH ($X\ ^3\Sigma^-$) + H (^2S) reaction represents a prototype for insertion reactions, which have attracted much recent interest.^{1–4} Because of its important role in atmospheric and combustion chemistry, the title reaction has been studied extensively in both experimental and theoretical fronts. Measurements of the canonical rate constant⁵ showed an Arrhenius-type temperature dependence, indicating an intrinsic barrier on the potential energy surface (PES). On the other hand, the product state distributions were found to be largely statistical,^{6–9} suggesting the existence of a reaction intermediate. Such an intermediate was recently confirmed by the nearly backward–forward symmetric angular distribution found in crossed molecular beam experiments.^{10–12}

This reaction has several unique features that distinguish it from the other prototypical insertion reactions. As shown in Figure 1, it has a small insertion barrier (~ 0.08 eV) in the entrance channel,^{13–15} while most other insertion reactions are barrierless.⁴ In addition, there exists an adiabatic abstraction pathway, which has a somewhat higher barrier (~ 0.2 eV), raising the possibility of two coexisting mechanisms. Finally, it has a large exothermicity (~ 1.25 eV), which renders the lifetime of the reaction intermediate relatively short. These properties might be responsible for deviations from a completely statistical paradigm.

Because of the involvement of light atoms, it is imperative to treat the dynamics quantum mechanically to account for quantum effects, such as zero-point energy and tunneling. Like other complex-forming reactions, however, a quantum mechanical (QM) treatment of the reaction dynamics is challenging in several aspects. First, it requires a large number of basis functions and grid points to converge the many quantum states

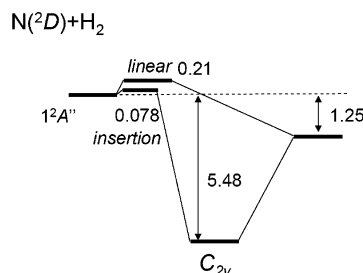


Figure 1. Energetics of the title reaction.

supported by the deep (~ 5.5 eV) NH_2 well. Second, the commonly used centrifugal sudden (CS) approximation^{16,17} may not be accurate because of the strong Coriolis coupling stemming from the floppy NH_2 complex. This is particularly true for the state-to-state attributes.¹⁸ Hence, an exact quantum treatment with the Coriolis coupling should be used. Finally, the reaction might be dominated by NH_2 resonances, so that a long propagation is needed in a wave packet treatment. So far, integral cross sections (ICSS) and rate constants have been reported using both approximate^{19–21} and exact wave packet methods.²² However, the only exact QM differential cross sections (DCSS) have until very recently been obtained using a time-independent body-frame hyperspherical coordinate method.^{11,12,18,23} Because the time-independent results are restricted to a few points in the energy axis, it is difficult to understand the dependence on energy. In addition, the previous QM results were obtained on the PES of Pederson et al.,¹³ rather than on the more accurate PES published by Ho et al.²⁴ The differences between the two PESs are quite significant, as we show below.

Exact QM studies are also important because they serve as benchmarks in testing approximate methods, such as the quasi-classical trajectory (QCT) method²⁵ and statistical models.^{26–28} A key issue with regard to the title reaction is the statistical nature of the dynamics. Due to the relatively short lifetime of the NH_2 complex, the DCS of the title reaction may not be

[†] University of New Mexico.

[‡] Universidad Complutense.

completely forward–backward symmetric,¹² which is in contrast to a symmetric one mandated by statistical models. Our recent exact QM calculations²² have also indicated that the statistical model overestimates the rate constant, presumably due to the relatively short lifetime of the NH₂ complex. On the other hand, the QCT model has been found to underestimate the rate constant values due apparently to the failure in accounting for tunneling.^{21,22}

Very recently, two of the authors proposed an accurate and efficient method to calculate the S-matrix elements of atom–diatom reactions,²⁹ which are needed to compute the DCS. This approach, which is similar in spirit to those proposed by several other groups,^{30,31} is based on the propagation of wave packets in the Chebyshev order domain.^{32,33} Like time-dependent wave packet methods,³⁴ the Chebyshev approach yields a column of the S-matrix and its dependence on energy, and scales pseudo-linearly with the dimension of the Hamiltonian matrix. With the implementation of OpenMP, this method has proven to be very efficient and capable of treating computationally challenging problems such as the title reaction.²⁹

In a previous publication,²⁹ we have reported preliminary results on the DCS for the title reaction up to 0.085 eV of collision energy, using the NH₂ PES of Ho et al.²⁴ In this paper, we provide details of our quantum calculation and extend the results to the collision energy of 0.2 eV, by including higher J partial waves. In addition, we compare the quantum results with QCT calculations on the same PES and explore mechanistic issues. This work is organized as follows. The next section (section II) provides details of the theoretical methods. The results are presented and discussed in section III. The final section (section IV) concludes.

II. Methods

A. Exact Quantum Approach Based on Chebyshev Propagation. Following our recent work,²⁹ the Hamiltonian is expressed in the product Jacobi coordinates ($\hbar = 1$)

$$\hat{H} = -\frac{1}{2\mu_R} \frac{\partial^2}{\partial R^2} - \frac{1}{2\mu_r} \frac{\partial^2}{\partial r^2} + \frac{\hat{j}^2}{2\mu_r r^2} + \frac{\hat{l}^2}{2\mu_R R^2} + V(R, r, \gamma) \quad (1)$$

where R and r are H–NH and N–H distances, respectively, and γ is the enclosing angle. The body-fixed (BF) frame is defined with the origin at the center of mass of the system and the z -axis along the R vector. μ_R and μ_r are the reduced masses associated with R and r coordinates, respectively. V corresponds to the potential of Ho et al.,²⁴ which is considered to be more accurate than its predecessor¹³ because more *ab initio* points were included in the fitting. \hat{j} and \hat{l} are operators of rotational and orbital angular momentum, respectively. In the current work, the non-adiabatic Renner–Teller effect^{35,36} is ignored because earlier work concluded that the A state of NH₂ does not play a significant role in thermal conditions.³⁵

The Hamiltonian was discretized using mixed finite basis representation/discrete variable representation (FBR/DVR).³⁷ For R and r , equidistant grids were defined and labeled by α_1 and α_2 . For the angular degrees of freedom, the following parity (p) adapted FBR was used:

$$|j\Omega; Jp\rangle = (2 + 2\delta_{\Omega,0})^{-1/2} (|J\Omega\rangle |j\Omega\rangle + p(-1)^J |J - \Omega\rangle |j - \Omega\rangle) \quad (2)$$

where $|j\Omega\rangle \equiv \Theta_{j\Omega}(\gamma, 0)$ are normalized associate Legendre functions with the Condon–Shortley phase convention³⁸ and

$|J\Omega\rangle = \sqrt{(2J+1)/(8\pi^2)} D_{\Omega,0}^{J*}$ represents the overall rotation, where $D_{\Omega,M}^J$ is the Wigner rotation matrix.³⁹ The projection of J and j onto the z -axis in the BF frame, Ω , is thus restricted to be non-negative. To summarize, the wave packet with a total angular momentum J and parity p was expressed as

$$|\psi^{Jp}\rangle = \sum_{\alpha_1 \alpha_2 j \Omega} \psi_{\alpha_1 \alpha_2 j \Omega}^{Jp} |\alpha_1 \alpha_2\rangle |j\Omega; Jp\rangle \quad (3)$$

To evaluate the action of the kinetic energy operators, we take advantage of the transformation between FBR and DVR. For example, the action of the first two kinetic energy terms in eq 1 was calculated using fast sine Fourier transform (sine FFT). When calculating the action of the rotational kinetic energy operators (third and fourth terms in eq 1), the FBR was used. Subsequently, the wave function was transformed to a pure DVR where the action of the potential energy operator was calculated. In this case, the DVR was defined by the angular Gauss–Legendre quadrature points associated with rotational basis $|j\Omega\rangle$. The angular DVR and FBR are related through a pseudospectral transform.^{40,41}

The S-matrix element from an initial state (i) to a final state (f) is expressed as a discrete Fourier transform of the cross-correlation functions:²⁹

$$S_{f-i}^{Jp}(E) = \frac{1}{2\pi\mathcal{H}^- \sin \vartheta} \sum_{k=0}^{\infty} (2 - \delta_{k,0}) e^{-ik\vartheta} C_k^{(f-i)} \quad (4)$$

where the Chebyshev angle is given by $\vartheta = \arccos E_{\text{scaled}}$,³² and $a_i(E)$, $a_f(E)$ are the energy amplitudes of the initial and final state wave packets, respectively. The correlation function is defined as follows:²⁹

$$C_k^{(f-i)} = \langle \varphi_{v_j f} | \langle JM j l_f | \psi_k(R=R_\infty) \rangle \quad (5)$$

where R_∞ is the location where the projection is made and $\varphi_{v_j f}$ is the product rovibrational wave function. The Chebyshev wave packet $|\psi_k\rangle = T_k(\hat{H}_{\text{scaled}})|\psi_0\rangle$ was propagated by a modified three-term Chebyshev recursion relationship:^{42,43}

$$|\psi_{k+1}\rangle = D(2\hat{H}_{\text{scaled}}|\psi_k\rangle - D|\psi_{k-1}\rangle) \quad (6)$$

with $|\psi_1\rangle = D\hat{H}_{\text{scaled}}|\psi_0\rangle$ and $|\psi_0\rangle = |\chi_i\rangle$. The following damping function D was applied at the grid edges:

$$D(R) = \begin{cases} 1 & \text{for } x \leq x_d, \\ e^{-d_c(x-x_d)^2} & \text{for } x > x_d \end{cases} \quad (x = R, r) \quad (7)$$

To avoid the divergence of the Chebyshev polynomials outside the range $[-1, 1]$, the Hamiltonian in eq 6 and the energy were properly scaled

$$\hat{H}_{\text{scaled}} = (\hat{H} - H^+)/H^- \quad (8a)$$

$$E_{\text{scaled}} = (E - H^+)/H^- \quad (8b)$$

Here, the spectral medium and half-width of the Hamiltonian $H^\pm = (H_{\text{max}} \pm H_{\text{min}})/2$ were calculated from the spectral extrema, H_{max} and H_{min} , which can be readily estimated.

The initial wave packet $|\psi_0\rangle = |\chi_i\rangle$ was taken as a product of a well-defined rovibrational eigenfunction $|\varphi_{v_j i}\rangle$ of the diatomic reactant H₂, a space-fixed angular momentum eigenstate in the coupled representation $(|JM j l_i\rangle)$, and a one-dimensional Gaussian-shaped wave packet along the N–H₂ translational coordi-

nate. In particular, the following form in the reactant Jacobi coordinates (R', r', γ') was used:

$$|\psi_0\rangle = N e^{-(R'-R_0)^2/2\delta^2} \cos k_0 R' |\varphi_{v_j}\rangle |JMj_i l_i\rangle \quad (9)$$

where k_0 , R'_0 , and δ are its mean momentum, position, and width, respectively, and N is the normalization constant. v_i and j_i stand for the vibrational and rotational quantum numbers of reactant di-atomic molecule (H_2), respectively. In practice, this wave function needs be transformed to the product Jacobi coordinates. Since the initial wave packet is real, the propagation in eq 6 can be carried out entirely with real algebra,³³ which represents significant savings over the complex time propagation.

The differential cross section is given by^{27,44}

$$\frac{d\sigma}{d\Omega}(\theta, E) = \frac{1}{8k_{v_j}^2} \frac{1}{(2j+1)} \sum_{\Omega_i, \Omega_f} [|f_+(\theta, E)|^2 + |f_-(\theta, E)|^2] \quad (10)$$

where θ is the scattering angle in the SF frame and

$$f_+(\theta, E) = \sum_{j_p} (2J+1) d_{\Omega_f, \Omega_i}^j(\pi - \theta) S_{v_j, \Omega_f \leftarrow v_j, \Omega_i}^{j_p}(E) \quad (11a)$$

$$f_-(\theta, E) = \sum_{j_p} p(2J+1) d_{\Omega_f, \Omega_i}^j(\theta) S_{v_j, \Omega_f \leftarrow v_j, \Omega_i}^{j_p}(E) \quad (11b)$$

where the j, Ω -specified S-matrix elements are obtained by a transformation between BF and SF frames:^{27,44}

$$S_{v_j, \Omega_f \leftarrow v_j, \Omega_i}^{j_p} = \sum_{l_i, l_f} (U_{l_i, \Omega_i}^{j_p})^* S_{v_j, l_f \leftarrow v_j, l_i}^{j_p} U_{l_f, \Omega_f}^{j_p} \quad (12)$$

with

$$U_{l_i, \Omega_i}^{j_p} = \frac{i^l}{\sqrt{2(1 + \delta_{\Omega, 0})}} [\langle j\Omega, J - \Omega | l0 \rangle + p(-1)^J \langle j - \Omega, J\Omega | l0 \rangle] \quad (13)$$

Here, $\langle \dots | \dots \rangle$ denotes the Clebsch–Gordan coefficients.³⁹

Finally, the state-to-state integral cross section (ICS) can be expressed as follows:

$$\sigma_{v_j, \Omega_f, v_j, \Omega_i}(E) = \frac{\pi}{(2j_i + 1)k_{v_j}^2} \sum_{J, p, l_i, l_f} (2J+1) |S_{v_j, \Omega_f \leftarrow v_j, \Omega_i}^{j_p}(E)|^2 \quad (14)$$

In our calculations, we only consider the reaction from the ground rovibrational state of the reactant: $H_2(j_i = 0, v_i = 0)$. Extensive convergence tests were carried out for the $J = 0$ case, and the same numerical parameters were employed in nonzero J calculations. Equidistant grids with 127 points were chosen for both $R \in (0.5, 15.0)a_0$ and $r \in (0.5, 15.0)a_0$, and 100 Gauss–Legendre quadrature points were chosen for $\gamma \in (0^\circ, 180^\circ)$. The rotational basis thus included all the numbers from $j = 0$ up to $j_{\max} = 99$. The initial wave packet was launched at $R'_0 = 9.0a_0$ with $\delta = 0.15a_0$ and $\hbar^2 k_0^2 / (2\mu R) = 0.12$ eV. The projection was carried out at $R_\infty = 8a_0$. To control the spectral range, the PES was cut off at 2.72 eV and the centrifugal potential energy term was cut off at 5.44 eV. The highest total angular momentum quantum number (J) was 25, which allowed the

convergence of the reaction cross section up to 0.2 eV of collision energy. A total of 10 000 steps of Chebyshev iterations were used.

B. Quasi-Classical Trajectory Approach. The quasi-classical trajectory method used for the calculations presented here has been described in previous publications (see, for instance, ref 25 and references therein), and only the details relevant to the present reaction will be given here.

In the present work, batches of 250 000 trajectories were run on the PES of Ho et al.²⁴ for the ground H_2 initial state ($j_i = 0, v_i = 0$) at the fixed collision energies 0.108, 0.145, 0.165, and 0.195 eV. Trajectories were started at a N– H_2 distance of 8.0 Å, and a time step of 0.05 fs was used for the integration of the equations of motion. Under these conditions, total energy was conserved to within four significant figures.

The rovibrational energies of the H_2 and NH molecules were calculated by semiclassical quantization of the action using the potential given by the asymptotic di-atom limits of the PES. These rovibrational energies were fitted to Dunham expansions containing 20 terms (fourth power in $v_i + 1/2$ and third power in $j_i(j_i + 1)$). The assignment of product quantum numbers (v_f, j_f) was carried out by equating the classical rotational angular momentum of the product molecule to $\sqrt{j_f(j_f+1)}$. With the (real) j_f value so obtained, the vibrational quantum number v_f was found by equating the internal energy of the outgoing molecule to the corresponding Dunham expansion. In the most common procedure, these real v_f and j_f values are rounded to the nearest integers, in what is named the histogramatic binning method. However, as in previous work,^{45,46} we have used a Gaussian-weighted binning procedure, in which a Gaussian function centered at the quantal action with a given width was used to weight the trajectories following the criteria that the closer the vibrational action of a given trajectory to the nearest integer, the larger the weighting coefficient for that trajectory. In the present work, we have used a full width at half-maximum for the Gaussian functions of 0.1.

The collision times of the trajectories, that is, the time elapsed between the strong interaction in the entrance and exit channels of the reaction have been calculated as $\tau_c = \tau_f - \tau_i - \tau_r$, where τ_i is the total time of the trajectory and τ_i and τ_f are the initial and final times, respectively, where the strong interaction starts in the reactants and ends in the products. The values of τ_i and τ_f were determined by defining previously a distance parameter for reagents and products, ρ_r and ρ_p , respectively, by plotting a significant number of trajectories to determine the point where the strong interaction starts and ends. In the present case, values of $\rho_r = \rho_p = 2.5$ Å have been employed. For more details see ref 4.

The collision energy evolution of the reaction probability at different values of the total angular momentum $J = 0, 5, 10, 15$, and 20, $P^J(E_c)$, for the title reaction has been calculated by running batches of 10^5 trajectories for each value of J in the collision energy range from threshold up to 0.26 eV as described in ref 25 using the expression

$$b = \frac{1}{\mu v_r} \sqrt{J(J+1)} \quad (15)$$

where b is the impact parameter of the trajectory and μ and v_r are the N– H_2 reduced mass and relative velocity, respectively. The method of moments expansion in Legendre polynomials has been employed to obtain the $P^J(E_c)$ from the trajectory results. The integration step size and the initial distance between

the incoming atom and the center-of-mass of the di-atomic were the same as in the batch at fixed collision energy mentioned above.

For the calculation of the excitation function, that is, the integral cross section as a function of collision energy, a batch of 5×10^5 trajectories was run with the same H₂ initial state and for randomly sampled collision energies, E_c , between the threshold and 0.25 eV. As in the calculations at fixed collision energies, trajectories were started at a N–H₂ distance of 8.0 Å, and a time step of 0.05 fs was used for the integration of the equations of motion. The maximum impact parameter, b_{\max} , for this insertion reaction increases with collision energy due to the presence of the barrier for C_{2v} geometry. Thus, the impact parameter for each trajectory at a given collision energy E_c was chosen by randomly sampling between zero and a maximum value $b_{\max}(E_c)$ given by the expression

$$b_{\max}(E_c) = D(1 - E_D/E_c)^{1/2} \quad (16)$$

where the parameters D and E_D were obtained previously by fitting the values of the maximum impact parameters found by running small batches of trajectories at several selected E_c to the functionality of eq 16. Over the range of E_c investigated, b_{\max} was always found to grow with E_c . The parameters used ensure that no reaction occurs at a given E_c for values of the impact parameter larger than $b_{\max}(E_c)$. With this kind of energy-dependent sampling of the maximum impact parameter, each trajectory was weighted by $w_i = b_{\max}^2/D^2$. The excitation functions, $\sigma_R(E_c)$, were subsequently calculated by the method of moments expansion in Legendre polynomials as described elsewhere.²⁵

III. Results and Discussions

A. Reaction probabilities and ICSs. We first focus on the QM initial state ($j_i = 0, v_i = 0$) specified total reaction probabilities, which were obtained by summing all open product channels. In Figure 2, the dependence of the total reaction probability on the collision energy is displayed for several selected J . It is immediately clear that the title reaction has an intrinsic threshold at $E_c \approx 0.05$ eV for $J = 0$. This threshold is smaller than the classical insertion barrier in the entrance channel (0.078 eV), underlining the importance of tunneling in this reaction. At larger J values, the reaction threshold shifts to larger collision energies because of the emergence of the centrifugal barrier. For all partial waves, the reactivity increases steadily above the corresponding thresholds. However, the probabilities never reach 100%, implying an appreciable nonreactive flux. Significant oscillations are seen in the figure, but the peaks are quite broad, indicating the dominance of relatively short-lived resonances. This picture is similar to the O (¹D) + H₂ reaction, where a deep well and large exothermicity are also present.^{47,48} For $J = 25$, the maximum total angular momentum chosen in this paper, the threshold energy is about 0.2 eV. This is thus taken as the upper limit for the cross section.

The QCT total reaction probabilities for the same J values are also displayed in Figure 2. The classical thresholds are higher and sharper than the corresponding quantum ones due to the inability of the QCT model to describe tunneling. Otherwise, the energy dependence is quite similar. It is interesting to note that both QM and QCT probabilities have a peak just above the reaction thresholds. We believe that this peak is due to the so-called bottleneck states near the top of the potential barrier,⁴⁹ similar to those found for the H + H₂ exchange reaction. Quantum mechanically, such a state can be considered as a

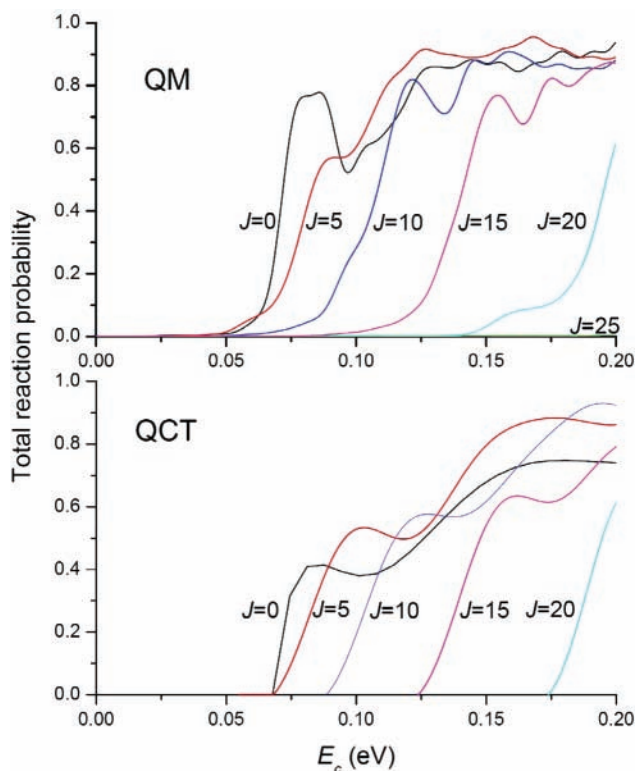


Figure 2. Energy dependence of initial state specified ($j_i = 0, v_i = 0$) QM (upper panel) and QCT (lower panel) total reaction probabilities for several selected J values.

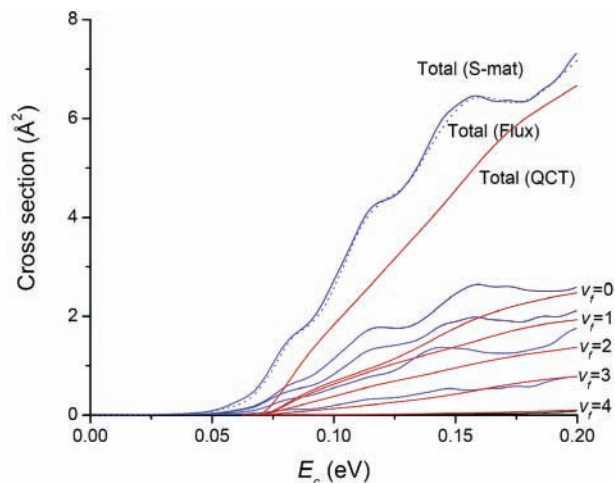


Figure 3. Energy dependence of initial state specified ($j_i = 0, v_i = 0$) total and vibrationally resolved ICSs obtained from both QM (blue) and QCT (red) methods. The QM ICS (dotted line) calculated using the flux method is also displayed for comparison.

resonance that localizes near the barrier. Classically, it reflects the fact that the trajectories spend a longer time near the barrier because of reduced kinetic energies. As discussed below, such peaks might be responsible for the oscillations in both the ICS and DCS for the reaction. Obviously, more detailed studies are needed to elucidate the nature of such resonances.

In Figure 3, we first compare the total QM ICSs as a function of collision energy that were obtained using the S-matrix method and a flux method⁵⁰ reported earlier,²² respectively. The agreement between the two curves (dotted and solid lines) obtained from two very different numerical methods is quite satisfactory. As expected, the total cross section generally increases with the increasing collision energy above the reaction threshold. This is consistent with the experimental measurement

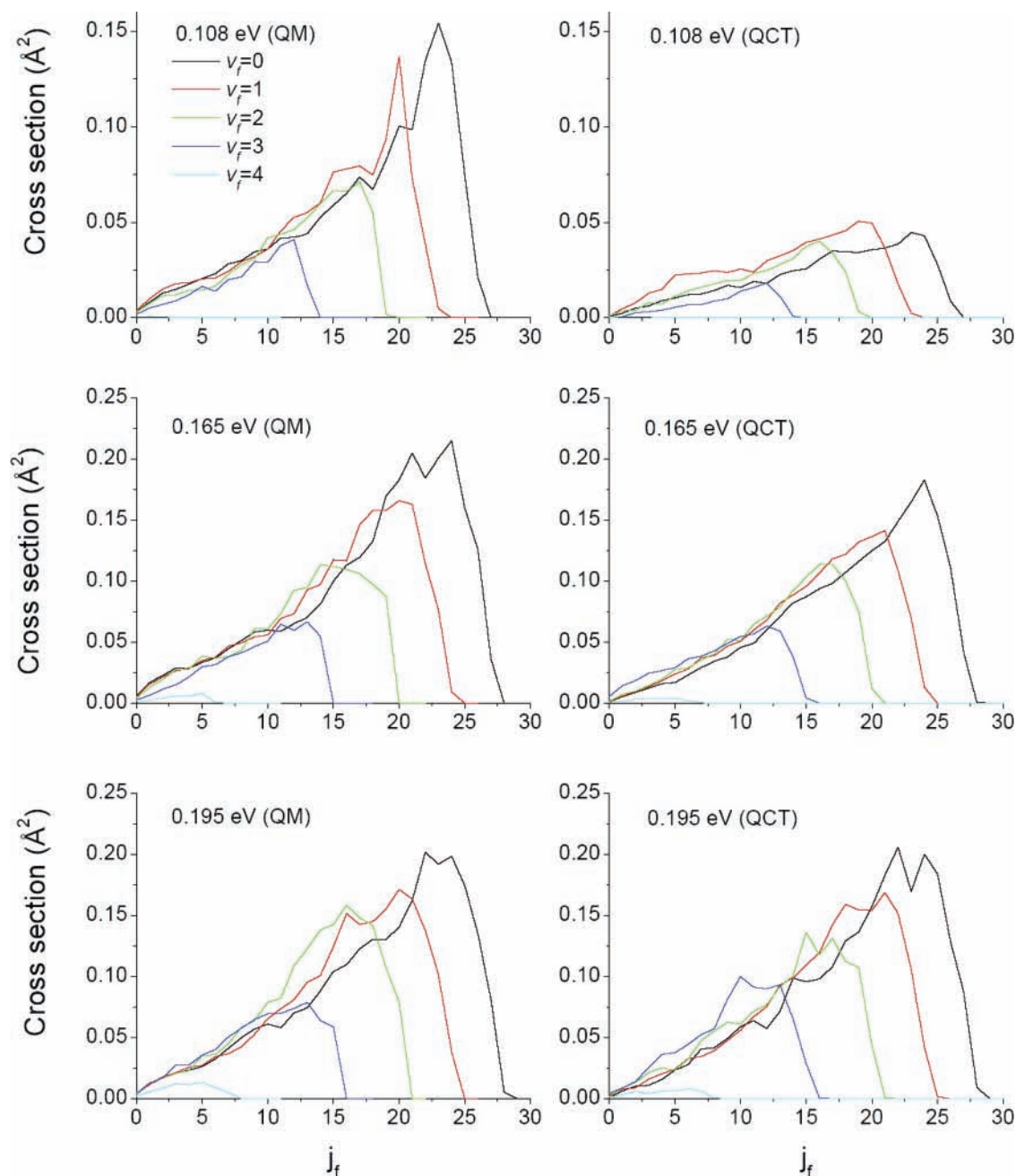


Figure 4. Initial state specified ($j_i = 0, v_i = 0$) and product rovibrationally resolved ICSs, for example, product rotational distributions, at several selected collision energies obtained from QM (left panels) and QCT (right panels) calculations.

of Liu.³ At 0.2 eV of collision energy, the cross section is approximately 7.5 \AA^2 . We note that the cross section is not featureless, and the mild oscillations might be due to short-lived resonances surviving the sum over the partial waves. In the same figure, the ICSs from the QCT calculations is also displayed. As expected, the classical ICS is smaller than the QM value at the same energy, reflecting the importance of the quantum tunneling effect. However, the agreement improves at higher collision energies. Also, the QCT cross section has much less structure.

Also shown in the Figure 3 are the QM and QCT vibrationally resolved ICSs, which were obtained by summing populations of all corresponding rotational states. For both results, it is clear that throughout the energy range the product vibrational state population decreases monotonically with increasing vibrational quantum number. Such a distribution reflects the fact that there are more rotational states in low-lying vibrational manifolds,

and it has been shown to be well described by statistical models.^{23,26} Notice how the agreement between QM and QCT ICSs improves markedly for the largest product vibrational states. The rovibrationally resolved ICSs (rotational distributions) are displayed in Figure 4 for several selected collision energies. In contrast to the product vibrational distribution, all the rotational distributions are inverted with peaks near the highest allowed rotational states. The QCT distributions are generally smaller and smoother than the QM ones, especially at the lowest collision energy, underscoring the importance of quantum effects. However, the agreement between QM and QCT results is striking at 0.195 eV collision energy. The non-inverted vibrational distribution and inverted rotational distribution of the NH product are consistent with the dominant insertion mechanism for the title reaction. The general trends observed here are also in reasonably good agreement with previous

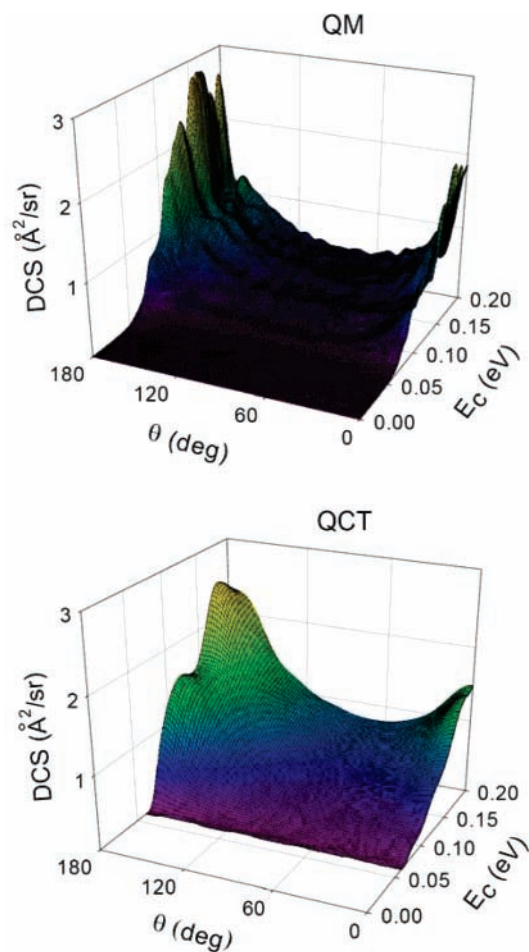


Figure 5. Three-dimensional plots of the initial state specified ($j_i = 0, v_i = 0$) total QM and QCT DCSs as a function of collision energy.

theoretical results on different PESs and with experimental data.^{12,13,18,23,26}

B. DCSs. In this section, we focus on DCSs of the title reaction and examine its dependence on the collision energy up to 0.2 eV. Figure 5 displays the total DCS as a function of collision energy obtained from both the QM and QCT calculations. As discussed earlier, the classical threshold is larger and sharper than the QM one, due to tunneling. Furthermore, the energy dependence of the QCT DCS is also smoother than that of the QM counterpart.

As expected, both angular distributions are peaked at two extreme angles (0° and 180°) at all energies, a typical feature for complex-forming reactions. However, it can also be noted that there is a strong bias in the backward direction ($\theta \approx 180^\circ$) in both the QM and QCT angular distributions. The asymmetry in DCS implies that the lifetime of the reaction intermediate (NH₂) may not be sufficiently long to render the reaction completely statistical. As discussed earlier, the relatively short lifetime for the NH₂ complex can presumably be attributed to the large exothermicity of the reaction. On the other hand, the backward bias in DCS could also stem from the contribution from the abstraction channel. This possibility will be discussed further below.

As shown in the figure, the QM DCS shows some oscillations with the collision energy. The oscillations appear to be more pronounced than those in the corresponding ICS (Figure 3) and are likely due to resonances, particularly those near the transition state. Similar oscillations are also seen in the QCT distributions, albeit much less pronounced. As mentioned earlier, we speculate

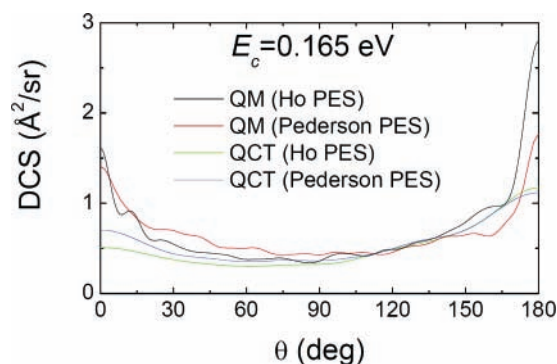


Figure 6. Comparison of the initial state specified ($j_i = 0, v_i = 0$) DCSs at 0.165 eV between QM and QCT calculations on the indicated PESs.

that these structures are due to bottleneck states near the barrier, but further investigations on the origin of these oscillatory features are needed.

In Figure 6, we compare the DCS obtained from the earlier QM and QCT results on the Pederson et al. PES at 0.165 eV^{11,12} with those obtained in this work on the Ho et al. PES. Both QM results show strong scattering in both forward and backward directions with a bias in the backward direction. However, the QM DCS on the PES of Ho et al. shows a much stronger backward scattering peak. Since both QM methods are exact in treating the dynamics, the observed differences in the DCS can only be attributed to the differences in the PESs used in the calculations. Because the PES of Ho et al. is deemed more accurate because of additional *ab initio* points included in the fit,²⁴ we believe the results presented in this work are more reliable.

Qualitatively consistent with the QM results discussed above, the DCS from QCT calculations on the Ho et al. PES has also a larger backward bias than that on the Pederson et al. PES. This reinforces the notion that the increased backward bias in the DCS is due to differences in the PESs. Interestingly, the QCT DCSs do not possess the sharp peaks at the angular extremes and seem to lack an important part of the forward hemisphere scattering as compared with the QM results. These differences have been noted before and were attributed to tunneling through the combined potential and centrifugal barrier that is missing in the QCT calculations.¹¹ Very recently Bonnet et al.⁵¹ have questioned this explanation and attribute the absence of sharp peaks in the QCT calculations to the fact that parity conservation is ignored in classical mechanics. Apparently, these same effects are present on the new PES of Ho et al. We note in passing that the sharp backward peak in the QM DCS is difficult to measure experimentally unless a high angular resolution can be achieved.

In Figure 7, we compare the vibrational state resolved DCSs from the QM and QCT calculations at three collision energies. Confirming the observations in Figures 3 and 4, the QM-QCT agreement improves steadily with increasing collision energy. Consistent with the ICSs in Figures 3 and 4, the DCS decreases monotonically with the vibrational quantum number at most scattering angles. However, the forward-backward symmetry or the lack thereof is different for each vibrational state. Interestingly, the lack of scattering in the forward hemisphere in the QCT DCSs decreases with increasing collision energy, and at 0.195 eV the agreement between QCT and QM DCSs is remarkably good for all product vibrational states. This trend would reinforce the explanation that the lack of forward hemisphere scattering is due to tunneling through the combined potential and centrifugal barrier.

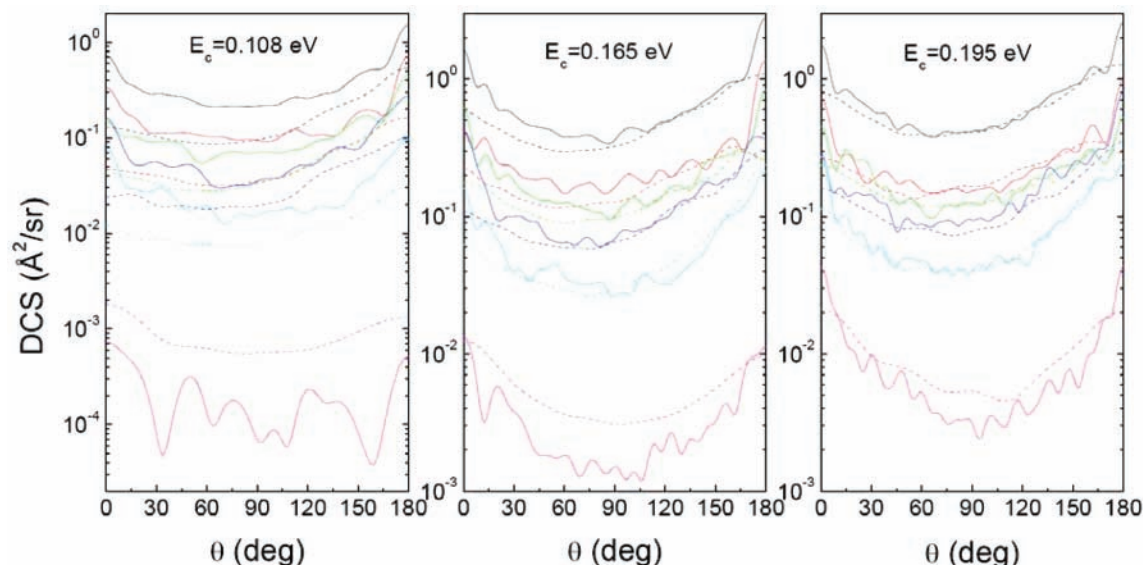


Figure 7. Comparison of the initial state specified ($j_i = 0, v_i = 0$) and product vibrational state resolved DCSs at three collision energies obtained from both QM (solid lines) and QCT (dashed lines) calculations. The total DCS and those for $v_f = 0, 1, 2, 3,$ and 4 are colored coded as black, red, green, blue, cyan, and purple.

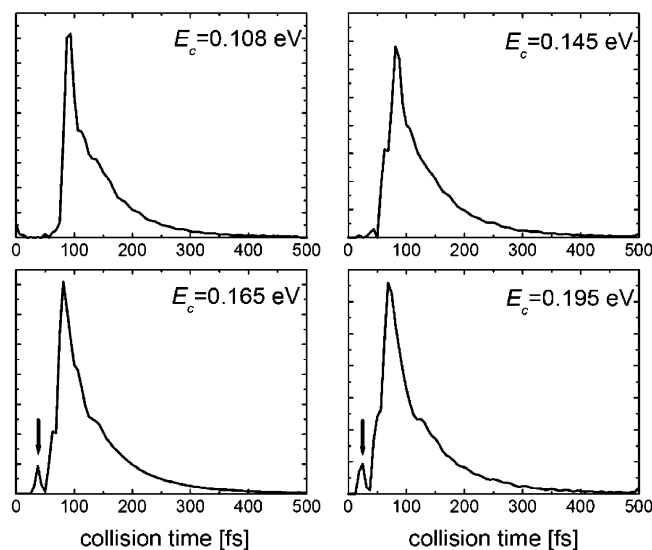


Figure 8. Collision time distributions of the NH_2 intermediate complex at different collision energies, obtained from the QCT calculations. The arrows indicate the presence of an abstraction channel.

C. Mechanism. To further understand the dynamics and mechanism of the title reaction, we have analyzed the collision time distribution of the NH_2 reaction intermediate from the trajectories. In Figure 8, the collision time distributions are displayed for four collision energies. As discussed earlier,⁴ the NH_2 intermediate is a relatively short-lived species, with a lifetime on the order of 100 fs. As expected, collision times decrease with increasing collision energy. The collision time profiles also shed light on the mechanism. The major peaks in Figure 7, for example, belong to the insertion trajectories, in which the incoming N atom is inserted into the internuclear axis of the H_2 molecule. The resulting NH_2 complex does not dissociate until the trajectory undergoes one or more bending motions, which are responsible for the highly excited product rotational distribution and the forward–backward symmetry in the DCS.

However, a closer look at the collision time distributions reveals a small peak that corresponds to a very fast component. This fast component becomes more important as energy

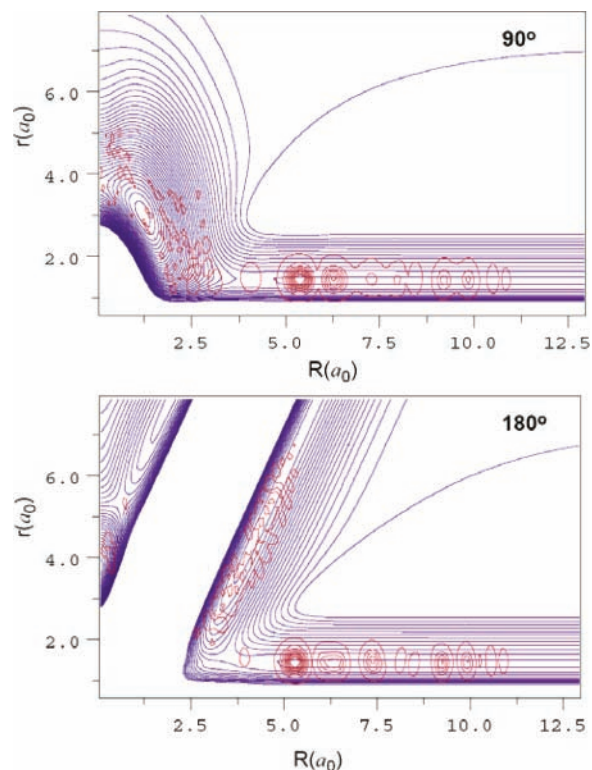


Figure 9. Contour map of the Chebyshev wave packet at $k = 4000$ steps of propagation at two Jacobi angles. The contours of the PES are superimposed on the wave packet. The left panel clearly indicates some portion of the wave packet proceeds through the collinear abstraction pathway.

increases. Analysis of the corresponding trajectories indicated that it stems from the abstraction pathway, which has a collinear barrier of 0.21 eV on the PES of Ho et al. Taking tunneling into account, the abstraction pathway might play a role in the energy range of this work and will surely participate at higher energies. Indeed, a small portion of the ($J = 0$) reactive wave packet does proceed through the collinear abstract pathway, as shown in Figure 9. However, it would be difficult to quantify the percentage of the abstraction flux because of the coherent nature of the wave packet.

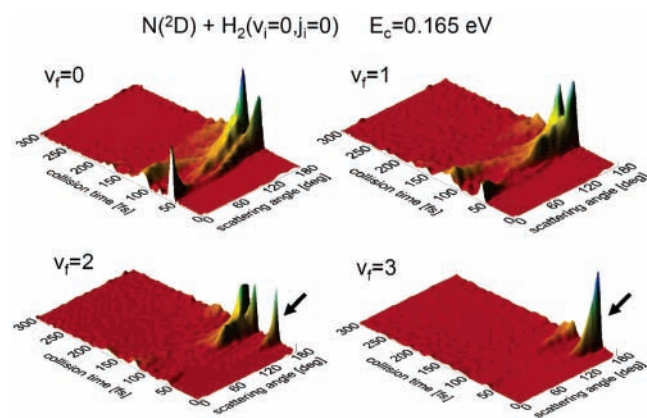


Figure 10. Vibrational state resolved product angular distributions as a function of collision time obtained from the QCT calculations. The arrows indicate the contributions from the abstraction channel.

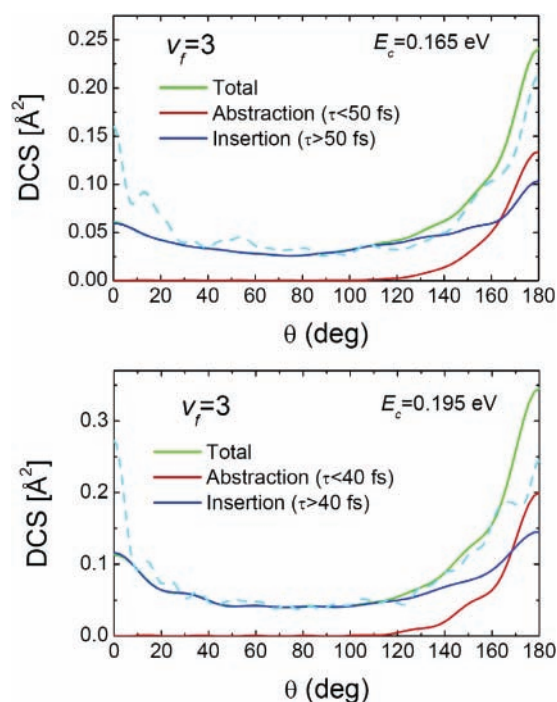


Figure 11. QM (cyan) and QCT (green) $v_f = 3$ DCSs at two collision energies. For the QCT DCS, the contributions from the abstraction channel (red) and insertion channel (blue) have been separated.

The abstraction reaction pathway involves a collinear barrier, rather than a potential well. As a result, it is very fast and will bias the backward scattering angles. Furthermore, the collinear location of the abstraction barrier also leads to high vibrational excitation in the product. This is clearly shown in Figure 10 where the product vibrational state angular distributions at $E_c = 0.165$ eV obtained from QCT are displayed as a function of collision time. For low-lying product vibrational states, the reaction flux starts out in the backward direction resulting from a single H–N–H bending motion and follows with forward scattering. This process repeats itself and eventually diminishes. On the other hand, the flux in the highly excited product vibrational states is dominated by a backward peak from the fast abstraction channel. Indeed, the backward bias is clearly seen in Figure 7 for the $v_f = 3$ channel, where the amount of the NH product produced by the insertion mechanism is small. Figure 11 depicts the QCT DCS in the $v_f = 3$ channel, where the contributions from abstraction and insertion trajectories have been separated, along with the corresponding QM DCS. As can

be seen, for trajectories with collision times shorter than 40–50 fs (abstraction trajectories), the DCS is backward biased, but for trajectories with collision times longer than 40–50 fs, the DCS is practically backward–forward symmetric with a slight backward bias.

Interestingly, the backward bias in the vibrational state resolved DCSs obtained from the QM calculations is not as pronounced as in the QCT results, especially at 0.195 eV collision energy. The origin of this discrepancy is not clear, but it can be expected that the abstraction mechanism will become more important as the collision energy increases. The coexistence of two rather different reaction mechanisms has been hotly debated before,^{13,52,53} but more work is needed to delineate them using exact QM methods. For the energies studied in this work, it is clear that the reaction is dominated by the insertion pathway.

IV. Conclusions

The title reaction has been investigated on the recent *ab initio* PES of Ho et al. using an exact quantum wave packet method and a QCT method. In particular, Coriolis coupled quantum mechanical calculations were carried out to obtain S-matrix elements for the initial H_2 state ($j_i = 0, v_i = 0$) with all J values up to 25, using a Chebyshev wave packet method. The differential and integral cross sections were obtained between 0 and 0.2 eV of collision energy. The results show that the title reaction produces NH products with a monotonical decay vibrational distribution and an inverted rotational distribution. The product angular distribution peaks at both backward and forward directions with a backward bias. The backward bias in the DCS is much more pronounced than that obtained previously on a less accurate PES. These results are qualitatively reproduced by the QCT method, although quantitative differences exist because of quantum effects such as tunneling. Further analysis of the wave packet and trajectories indicate that the reaction is dominated by the insertion mechanism but the abstraction mechanism also plays a role in high energies.

A distinct feature of the current work is the unraveling of the energy dependence of the fully state resolved cross sections. Both QM and QCT results indicate mild oscillations in both the ICS and DCS with respect to energy. These oscillations are attributed to short-lived resonances near the entrance channel barrier, which might serve as the quantum bottleneck states and regulate the reactive flux. These theoretical predictions call for more detailed theoretical investigations on these features, as well as quantum state resolved experimental measurements of the energy dependence of the DCS. In addition, we note that recent studies^{21,22} have identified possible inaccuracies of the Ho et al. PES. So a revamp of the PES might be needed to achieve a quantitatively accurate characterization of the reaction dynamics of this prototypic complex-forming reaction.

Acknowledgment. This work was supported by the DOE (Grant DE-FG02-05ER15694) and by the Spanish Ministry of Education and Science through Grant Number CTQ2005-08493-C02-01.

References and Notes

- (1) Casavecchia, P.; Balucani, N.; Alagia, M.; Cartechini, L.; Volpi, G. *Acc. Chem. Res.* **1999**, *32*, 503.
- (2) Liu, K. *Annu. Rev. Phys. Chem.* **2001**, *52*, 139.
- (3) Liu, K. *Int. Rev. Phys. Chem.* **2001**, *20*, 189.
- (4) Aoi, F. J.; Bañares, L.; Herrero, V. J. *J. Phys. Chem. A* **2006**, *110*, 12546.

- (5) Suzuki, T.; Shihira, Y.; Dato, T.; Umemoto, H.; Tsunashima, S. *J. Chem. Soc., Faraday Trans.* **1993**, 89, 995.
- (6) Umemoto, H.; Matsumoto, K. *J. Chem. Phys.* **1996**, 104, 9640.
- (7) Umemoto, H.; Asai, T.; Kimura, Y. *J. Chem. Phys.* **1997**, 106, 4985.
- (8) Umemoto, H. *Chem. Phys. Lett.* **1998**, 292, 594.
- (9) Umemoto, H.; Terada, N.; Tanaka, K. *J. Chem. Phys.* **2000**, 112, 5762.
- (10) Alagia, M.; Balucani, N.; Cartechini, L.; Casavecchia, P.; Volpi, G. G.; Pederson, L. A.; Schatz, G. C.; Lendvay, G.; Harding, L. B.; Hollebeek, T.; Ho, T.-S.; Rabitz, H. *J. Chem. Phys.* **1999**, 110, 8857.
- (11) Balucani, N.; Cartechini, L.; Capozza, G.; Segoloni, E.; Casavecchia, P.; Volpi, G. G.; Aoiz, F. J.; Bañares, L.; Honvault, P.; Launay, J.-M. *Phys. Rev. Lett.* **2002**, 89, 013201.
- (12) Balucani, N.; Casavecchia, P.; Bañares, L.; Aoiz, F. J.; Gonzalez-Lezana, T.; Honvault, P.; Launay, J.-M. *J. Phys. Chem. A* **2006**, 110, 817.
- (13) Pederson, L. A.; Schatz, G. C.; Ho, T.-S.; Hollebeek, T.; Rabitz, H.; Harding, L. B.; Lendvay, G. *J. Chem. Phys.* **1999**, 110, 9091.
- (14) Qu, Z.-W.; Zhu, H.; Schinke, R.; Adam, L.; Hack, W. *J. Chem. Phys.* **2005**, 122, 204313.
- (15) Varandas, A. J. C.; Poveda, L. A. *Theor. Chem. Acc.* **2006**, 116, 404.
- (16) Pack, R. T. *J. Chem. Phys.* **1974**, 60, 633.
- (17) McGuire, P.; Kouri, D. J. *J. Chem. Phys.* **1974**, 60, 2488.
- (18) Honvault, P.; Launay, J.-M. *J. Chem. Phys.* **1999**, 111, 6665.
- (19) Defazio, P.; Petrongolo, C. *J. Theor. Comput. Chem.* **2003**, 2, 547.
- (20) Chu, T.-S.; Han, K.-L.; Varandas, A. J. C. *J. Phys. Chem. A* **2006**, 110, 1666.
- (21) Varandas, A. J. C.; Chu, T.-S.; Han, K.-L.; Caridade, P. J. S. B. *Chem. Phys. Lett.* **2006**, 421, 415.
- (22) Lin, S. Y.; Guo, H. *J. Chem. Phys.* **2006**, 124, 031101.
- (23) Bañares, L.; Aoiz, F. J.; Gonzalez-Lezana, T.; Herrero, V. J.; Tanarro, I. *J. Chem. Phys.* **2005**, 123, 224301.
- (24) Ho, T.-S.; Rabitz, H.; Aoiz, F. J.; Bañares, L.; Vazquez, S. A.; Harding, L. B. *J. Chem. Phys.* **2003**, 119, 3063.
- (25) Aoiz, F. J.; Bañares, L.; Herrero, V. J. *J. Chem. Soc., Faraday Trans.* **1998**, 94, 2483.
- (26) Rackham, E. J.; Huarte-Larranaga, F.; Manolopoulos, D. E. *Chem. Phys. Lett.* **2001**, 343, 356.
- (27) Rackham, E. J.; Gonzalez-Lezana, T.; Manolopoulos, D. E. *J. Chem. Phys.* **2003**, 119, 12895.
- (28) Lin, S. Y.; Guo, H. *J. Chem. Phys.* **2004**, 120, 9907.
- (29) Lin, S. Y.; Guo, H. *Phys. Rev. A* **2006**, 74, 022703.
- (30) Althorpe, S. C. *J. Chem. Phys.* **2001**, 114, 1601.
- (31) Hankel, M.; Smith, S. C.; Allan, R. J.; Gray, S. K.; Balint-Kurti, G. G. *J. Chem. Phys.* **2006**, 125, 164303.
- (32) Chen, R.; Guo, H. *J. Chem. Phys.* **1996**, 105, 3569.
- (33) Gray, S. K.; Balint-Kurti, G. G. *J. Chem. Phys.* **1998**, 108, 950.
- (34) Zhang, J. Z. H. *Theory and Application of Quantum Molecular Dynamics*; World Scientific: Singapore, 1999.
- (35) Pedersen, L.; Schatz, G. C.; Hollebeek, T.; Ho, T.-S.; Rabitz, H.; Harding, L. B. *J. Phys. Chem. A* **2000**, 104, 2301.
- (36) Santoro, F.; Petrongolo, C.; Schatz, G. C. *J. Phys. Chem. A* **2002**, 106, 8276.
- (37) Light, J. C.; Carrington, T., Jr. *Adv. Chem. Phys.* **2000**, 114, 263.
- (38) Condon, E. U.; Shortley, G. H. *The Theory of Atomic Spectra*; Cambridge University Press: London, 1964.
- (39) Zare, R. N. *Angular Momentum*; Wiley: New York, 1988.
- (40) Corey, G. C.; Lemoine, D. *J. Chem. Phys.* **1992**, 97, 4115.
- (41) Corey, G. C.; Tromp, J. W. *J. Chem. Phys.* **1995**, 103, 1812.
- (42) Mandelshtam, V. A.; Taylor, H. S. *J. Chem. Phys.* **1995**, 102, 7390.
- (43) Mandelshtam, V. A.; Taylor, H. S. *J. Chem. Phys.* **1995**, 103 (8), 2903.
- (44) Zhang, J. Z. H.; Miller, W. H. *J. Chem. Phys.* **1989**, 91, 1528.
- (45) Bañares, L.; Aoiz, F. J.; Honvault, P.; Bussery-Honvault, B.; Launay, J.-M. *J. Chem. Phys.* **2003**, 118, 565.
- (46) Bañares, L.; Aoiz, F. J.; Honvault, P.; Launay, J.-M. *J. Phys. Chem. A* **2004**, 108, 1616.
- (47) Gray, S. K.; Goldfield, E. M.; Schatz, G. C.; Balint-Kurti, G. G. *Phys. Chem. Chem. Phys.* **1999**, 1, 1141.
- (48) Lin, S. Y.; Guo, H. *Chem. Phys. Lett.* **2004**, 385, 193.
- (49) Skodje, R. T.; Yang, X. *Int. Rev. Phys. Chem.* **2004**, 23, 253.
- (50) Lin, S. Y.; Guo, H. *J. Phys. Chem. A* **2004**, 108, 2141.
- (51) Bonnet, L.; Larrégaray, P.; Rayez, J.-C.; González-Lezana, T. *Phys. Chem. Chem. Phys.* **2006**, 8, 3951.
- (52) Dodd, J. A.; Lipson, S. J.; Flanagan, D. J.; Blumberg, W. A. M.; Person, J. C.; Green, B. D. *J. Chem. Phys.* **1991**, 94, 4301.
- (53) Kobayashi, K.; Takayanagi, T.; Tsunashima, S. *Chem. Phys. Lett.* **1997**, 277, 20.